Sustainable Energy & Fuels

Tuning the Oxidation State of SnOx and Mass Transport to Enhance Catholyte-Free CO2-to-Formate Electrolysis

Journal:	*Sustainable Energy & Fuels*
Manuscript ID	SE-ART-02-2023-000214.R2
Article Type:	Paper
Date Submitted by the Author:	26-May-2023
Complete List of Authors:	Kim, Taewoo; University of California, San Diego, Department of Nanoengineering; UC San Diego Devalla, Vivek; University of California San Diego, Nanoengineering Dunfield, Sean; University of California San Diego, Nanoengineering Palmer, Jack; UC San Diego, Dorr, Sara; University of California San Diego, Nanoengineering Kodur, Moses; University of California San Diego, Nanoengineering Gupta, Apoorva; University of California San Diego, Nanoengineering Fenning, David; University of California San Diego,

ARTICLE

Tuning the Oxidation State of SnO_x and Mass Transport to Enhance Catholyte-Free CO_2-to-Formate Electrolysis

Received 00th January 20xx,
Accepted 00th January 20xx

DOI: 10.1039/x0xx00000x

Taewoo Kim,[a] Vivek S. Devalla,[a] Sean P. Dunfield,[b] Jack R. Palmer,[c] Sara Dorr,[a] Moses Kodur,[a] Apoorva Gupta,[b] and David P. Fenning*[a,b,c]

Electrochemical CO_2 conversion to formate is a promising potential pathway to facilitate carbon neutrality with industrial feasibility. However, designing an active catalyst and optimizing the CO_2 electrolyzer to enable energy-efficient CO_2 conversion is a continuing challenge. Herein, we demonstrate that the initial surface oxidation state of tin oxide (SnO_x) catalysts is a key and enduring factor in determining the CO_2-to-formate conversion efficiency. Comparing the selectivity and energy efficiency of formate generation on thermally-evaporated and annealed SnO_x catalysts reveals that catalysts that are initially SnO-rich at the surface show improved overall efficiency relative to catalysts that are initially SnO_2-rich. Moreover, we show that controlling the flow rate of CO_2 strongly affects overall CO_2-to-formate conversion activity in partially-concentrated CO_2 streams in a catholyte-free electrolyzer, which emphasizes the importance of mass transport of CO_2 to design an efficient CO_2 electrolyzer. These findings provide insights into the critical importance of the chemical state in non-stoichiometric transition metal oxide catalysts like SnO_x catalysts and CO_2 mass transport for CO_2-to-formate conversion, offering fundamental guidelines and an efficient carbon-negative CO_2 conversion.

Introduction

Electrochemical CO_2 transformation is an attractive possibility to move toward carbon neutrality and introduce a new route to supply valuable carbonaceous chemicals. With the emerging penetration of intermittent renewable energy into the grid, electrochemical recycling of waste CO_2 can also offer larger-scale storage of renewable energy in chemical bonds.[1,2] Among possible value-added electrochemical CO_2 conversion products, formate is of particular interest to meet net negative carbon emissions[3] since electrochemical synthesis of formate requires less energy and fewer electron transfers than producing multi-carbon products. Moreover, integrating the electrosynthesized formate into formic acid fuel cells would enable formate to act as an alternative energy-dense carrier.[4]

Sn based catalysts are some of the most attractive for electrochemical CO_2-to-formate conversion. Sn has near optimal binding energy of *OCHO rather than *COOH,[5] which suppresses the reaction path toward CO, hydrocarbon, or alcohols. Also, its low cost could be an advantage for large-scale application.[6] Comparing the overall activity of CO_2-to-formate, it has been demonstrated that oxide-derived Sn catalysts show improved Faradaic efficiency and geometric current density of formate relative to metallic Sn catalysts.[7] It has also been reported that a catalyst surface where SnO and SnO_2 co-exist shows improved Faradaic efficiency in batch-type reactors as compared to a surface where only SnO_2 or metallic Sn is present.[8–10] Despite these insights, an industrially feasible electrochemical CO_2-to-formate system has yet-to-be-developed due to lack of integration of fundamental understanding of catalyst materials and electrolysis systems. A bottleneck has arisen from the mass transport limitation of CO_2 to the catalytically active sites in conventional electrolyzers using an aqueous catholyte.

Many efforts have been made to understand the reaction mechanisms in batch-type electrochemical reactors by relying on solubilized CO_2 in an aqueous electrolyte,[11] but larger-scale operations that require high current density are limited due to the low solubility of CO_2.[12,13] To overcome this solubility issue, a gas diffusion layer (GDL) has been utilized in a flow cell type electrolzyer to facilitate the direct feed of gaseous CO_2 to the electrode surface where the catalyst layer and an electrolyte interfaces.[14,15] In addition, a nano-structuring catalyst with high hydrophobicity is suggested to enhance CO_2 mass transport to the catalytic sites and circumvent electrolyte flooding.[16] Due to the necessity of multiple engineering aspects to a flow cell type electrolyzer, proper methods for performance evaluation are also required.[17] However, the electrolyte in the cathode chamber inevitably dilutes the liquid-phase products, necessitating a separation process. To date, membrane electrode assembly (MEA) type electrolyzers where the cathode and membrane contact without a catholyte (catholyte-free) have been considered as a promising alternative, although further work is necessary to understand engineering

[a] Chemical Engineering Program, Department of Nanoengineering, University of California San Diego, La Jolla, California, 92093, United States
[b] Department of Nanoengineering, University of California San Diego, La Jolla, California 92093, United States
[c] Materials Science & Engineering Program, University of California San Diego, La Jolla, California 92093, United States
† Electronic Supplementary Information (ESI) available. See DOI: 10.1039/x0xx00000x

parameters for larger-scale device performance.[18–21] Especially, there is a lack of experimental demonstration to bridge the fundamental insights of CO_2-to-formate conversion in a batch-type reactor to a catholyte-free electrolyzer, where a different reaction environment is present. Additionally, investigation into how partially concentrated CO_2 streams affect the overall catalytic activity is necessary as flue gasses generally contain less than 15% of CO_2.[22]

In this work, we report a strategy to enhance electrochemical conversion of CO_2 to formate in a catholyte-free electrolyzer via modulation of the initial oxidation state of the SnO_x catalyst and controlling mass transport of the CO_2 stream. Controlling this oxidation state is crucial, as improved Faradaic efficiency toward formate is shown with overall cell voltages in the range from 3.0 to 3.4 V on SnO_x layers with increased SnO relative to SnO_2 at the surface of the prepared catalyst (83 vs 74% FE, respectively). The calculated energy efficiency also improves to 36% at 3.0 V cell voltage on SnO_x catalyst layers with increased SnO present at the surface initially. Additionally, we show that with a partially concentrated CO_2 stream, as is present in flue gas compositions, the geometric partial current density of formate is suppressed with decreasing CO_2 concentration as expected. This lower CO_2 mass transport can be overcome by increasing flow rate of CO_2 stream, resulting in improved reaction kinetics. This work demonstrates that the energy efficiency and activity of electrochemical CO_2 reduction to formate on SnO_x layers can be promoted by modulating the initial oxidation states and flow rate of CO_2 stream even at low CO_2 concentration.

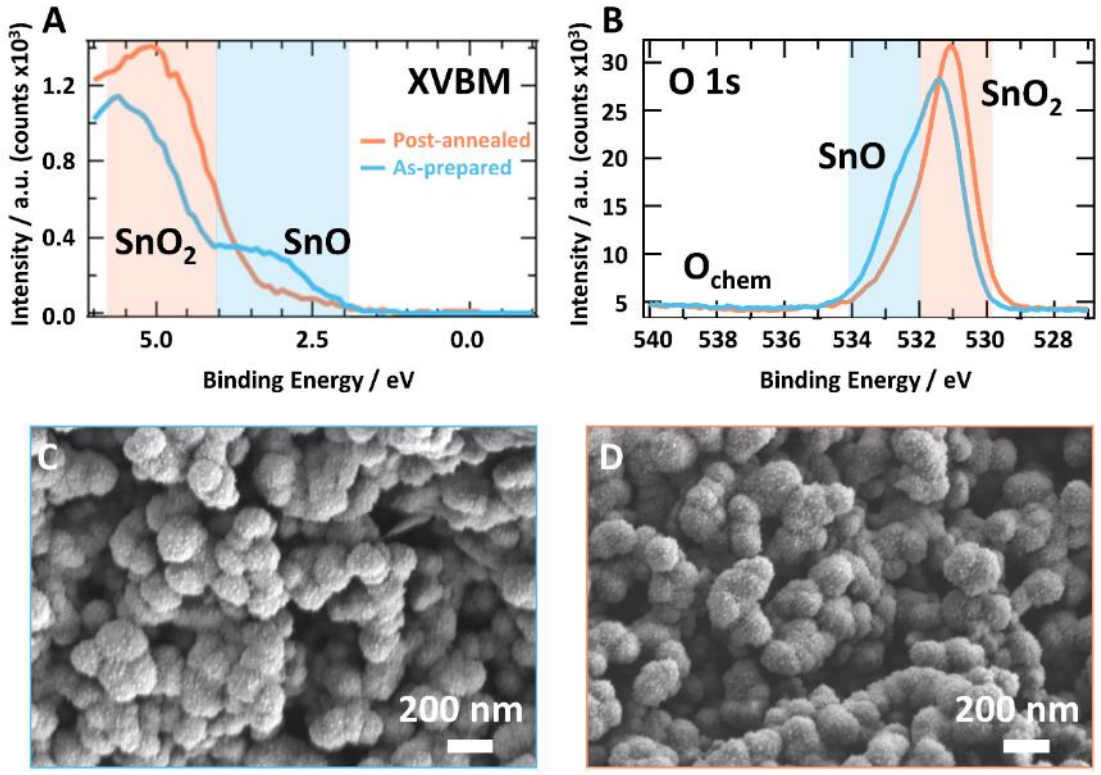

Figure 1. Properties of the SnO_x electrodes pre-electrolysis. X-ray photoelectron spectroscopy (XPS) of (A) X-ray valence band maximum (XVBM) and (B) O 1s core level spectra. As-prepared in blue and post-annealed in orange. Scanning electron microscopy (SEM) images of (C) as-prepared and (D) post-annealed SnO_x electrodes.

Results and discussion

Controlling Chemical States of SnO_x Layer

124±2 nm thick SnO_x catalyst layers were thermally evaporated onto the GDL, as determined by spectroscopic ellipsometry of films deposited by the same process on glass. In an effort to modulate the oxidation state of Sn, post-deposition annealing at 300 °C for 5 hrs in air was applied for comparison against un-annealed "as-prepared" catalyst layers. The corresponding oxidation states are confirmed via X-ray photoelectron spectroscopy (XPS). To highlight changes in the initial SnO_x oxidation state, both the X-ray valence band maxima (XVBM) spectra and O 1s core levels are shown in Figure 1A and 1B, respectively. Background-offset core level spectra and normalized core level spectra of the SnO_x films before and after

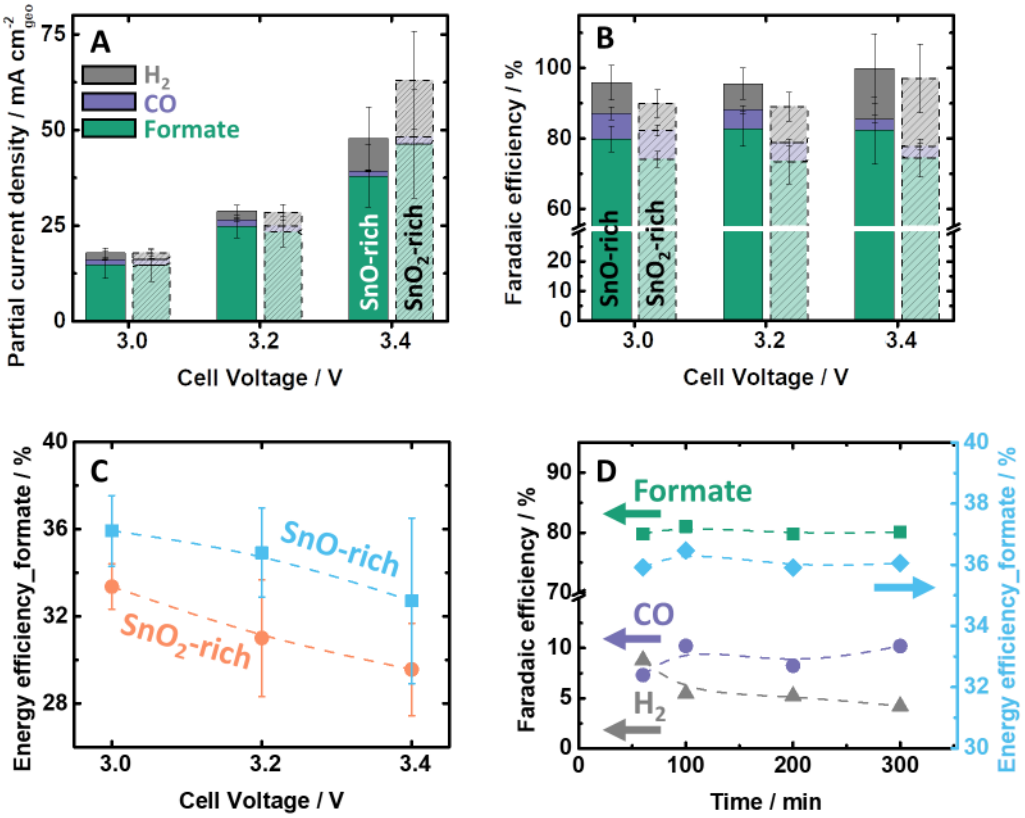

Figure 2. CO_2 reduction activity, selectivity, and efficiency of SnO-rich and SnO_2-rich catalysts as a function of cell voltage and time. (A) Geometric partial current densities and (B) Faradaic efficiencies of hydrogen, CO, and formate where filled boxes indicate catalysts prepared with a SnO-rich surface and the dashed box with light color is for the SnO_2-rich catalyst. (C) Energy efficiency of formate production for the catalysts prepared with SnO- and SnO_2-rich surfaces. The error bar indicates standard deviation from 3-5 electrolyses per cell voltage and per SnO-rich/SnO_2-rich sample, with each electrolysis running 1 hour. (D) Long-term electrolysis on the SnO-rich catalyst at 3.0 V of cell voltage.

electrolysis are included in Figure S1 and S2, respectively, while background-offset data for the GDL layer is included in Figure S3. Here, qualitative observations regarding the XVBM and the core level spectra (i.e., O 1s and Sn $3d_{5/2}$) are discussed rather than a peak deconvolution analysis due to the fact that: 1) signals from carbonaceous species from the GDL and the intermediate oxidation of SnO_x fall within ~1 eV in O 1s spectrum and 2) the marginal difference of binding energy between SnO and SnO_2 in Sn $3d_{5/2}$ spectrum makes it intrinsically difficult to deconvolute. As shown in Figure 1A, the XVBM spectra for the as-prepared layer shows two characteristic features, one for SnO at lower binding energy and one for SnO_2 at higher binding energy.[23,24] In contrast, the spectra for post-annealed layers reveals only a SnO_2 band edge. These observations are further corroborated by the O 1s spectra (Figure 1B), which show increased signal in the higher binding energy region of the as-prepared layers than post-annealed layers, where SnO and various other oxygenated contaminates would be expected. Together, these observations provide firm evidence that a post-heat treatment converts the mixed SnO-SnO_2 layer on the as-prepared layer (hereafter denoted SnO-rich) to a SnO_2-rich layer, consistent with our previous work on evaporated SnO_x thin films.[25] We note that semiconducting metal oxide layers grown through thermal evaporation often exhibit oxygen deficiencies.[26,27]

While the heat treatment appears to change the oxidation state of the SnO_x layer, we find that surface morphology is sustained during calcination. In both cases, the SnO_x electrodes shows spherical particles with gaps between the features (Figure 1C-D), similar to the surface structure of the GDL (Figure S4). We find a slight increase in the thickness of the SnO_x layer after heat treatment (135±3 nm), which is likely due to the volume expansion of the SnO_x upon heat treatment.[28,29] The annealing temperature was chosen to avoid changes in the contact angles of H_2O on the annealed GDL surfaces to ensure no structural changes on the GDL during heat treatment (Figure S5). Additionally, no distinguishable diffraction peaks from the SnO_x are detected by thin-film X-ray diffractometry (XRD) regardless of heat treatment and CO_2 electrolysis as shown in Figure S6, suggesting that the layers are at most poorly crystalline.

ARTICLE

Effect of the Chemical State of SnO_x Catalysts on the CO_2 Electrolysis

Shifting the initial oxidation state of the SnO_x catalyst modulates the CO_2 reduction performance as shown in Figure 2. In the range of cell voltage from 3.0 to 3.4 V, formate is the major CO_2 reduction product with marginal formation of CO and hydrogen on either of the SnO_x catalysts (Figure 2A). The calculated geometric partial current density of formate based on the chronoamperometry (Figure S7) on the SnO-rich catalyst increases with higher cell voltage (from 3.0 to 3.4 V) up to 34.9 mA cm^{-2}, while that of CO is rather consistent (< 1.6 mA cm^{-2}). In contrast, the SnO_2-rich catalyst shows similar activities for hydrogen and CO, and slightly more activity of formate generation at 3.4 V of cell voltage (46.3 mA cm^{-2}). We note that although the parasitic hydrogen evolution tends to increase with higher cell voltage on both SnO_x catalysts, formate is the dominant product. This indicates that: 1) the SnO_x catalysts prepared in this work are active for CO_2-to-formate reaction and 2) the limited mass transport of CO_2 may enhance hydrogen evolution at higher overpotentials.

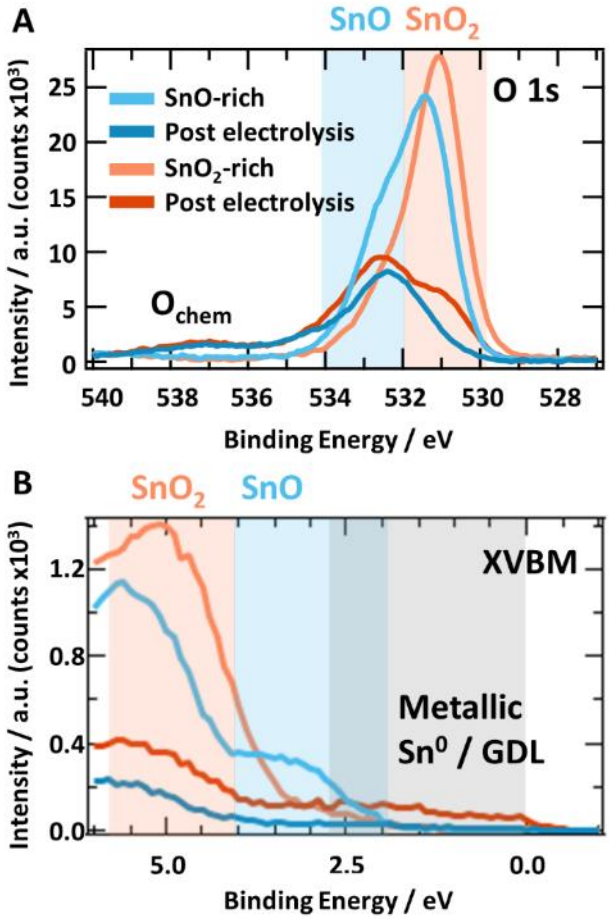

Figure 3. XPS spectra of (A) O 1s and (B) XVBM on SnO_x catalysts after 1 hr of CO_2 electrolysis at 3.0 V of cell voltage.

We find that the catalyst prepared with an SnO-rich surface shows improved selectivity toward formate as compared to the SnO_2-rich catalyst, as shown in Figure 2B. Specifically, Faradaic efficiency of formate on the SnO-rich catalysts appears to be 80.0~82.7% across all applied cell voltages. Meanwhile, we find that the Faradaic efficiency of CO and hydrogen trend in opposite directions as a function of voltage, with maximum Faradaic efficiencies of 7.3% and 13.0% at 3.0 and 3.4 V of cell voltage, respectively. In contrast, on the SnO_2-rich catalysts, Faradaic efficiency of formate is suppressed down to ~74.0% across all applied cell voltages. Similar to the SnO-rich catalyst, Faradaic efficiencies of CO and hydrogen trend in opposite directions, which suggests that CO and hydrogen formation on the SnO_x catalysts are sensitive to the cell voltage while formate generation is rather governed by the initial oxidation state of SnO_x. We note that the observed Faradaic efficiency and geometric partial current density of formate on the SnO-rich catalyst is comparable with the state-of-the-art catalysts (Figure S8).[18,21,30] Furthermore, the concentration of formate product by the catalyst prepared with a SnO-rich surface increases from 0.12 to 0.26 M with increasing cell voltage (Figure S9), which is about double the concentration produced in a state-of-the-art solid-electrolyte architecture in the low current/low load regime (<50 mA cm^{-2}).[21]

The corresponding energy efficiency of formate in Figure 2C shows that the catalysts prepared with a SnO-rich surface outcompete the catalysts prepared with a SnO_2-rich surface over the range of cell voltage, with a maximum of 36.0% energy efficiency at 3.0 V of cell voltage. This catalytic activity offers a possible nearest-term path to carbon-negative CO_2 electrolysis, based upon technoeconomic analysis indicating net carbon negative conversion at this efficiency with the current carbon intensity of the grid in California (0.2 $mTCO_2$/MWh).[3,31]

The SnO-rich catalyst shows stable Faradaic efficiency and energy efficiency of formate over an extended period of electrolysis at the fixed cell voltage (3.0 V), as shown in Figure 2D. The Faradaic efficiency and energy efficiency of formate remain essentially unchanged (80.2±0.5% and 36.1±0.2%, respectively) while the Faradaic efficiencies of CO and hydrogen show opposite trends as a function of electrolysis time. The Faradaic efficiency of CO gradually increases from 7.3% to 10.2% while that of hydrogen decreases from 8.8% to 4.2%. We speculate that the formation of CO and hydrogen is sensitive not only to the cell voltage but also to the morphology of the

catalyst. The post-electrolysis SEM images in Figure S10 indicate some agglomeration of SnO_x particles (~ 480±120 nm) after extended period of electrolysis as compared to the one after 1 hr electrolysis (~212±72 nm), as shown in Figure S14. This is supported by the current density profile during extended electrolysis (Figure S11), which shows a decay over time that is likely due in part to the agglomeration of SnO_x particles that decreases surface area. Despite the tendency toward agglomeration, we highlight that the formate generation on the SnO-rich catalyst is stable in extend electrolysis, as supported by the stable FE for formate (Figure 2D). Although a more reduced SnO_x (Figure S1-2) evolves during electrolysis, the impact of the initial oxidation state of the SnO_x catalyst is clear in the systematically differing activity and Faradaic efficiency of the SnO-rich vs SnO_2-rich catalysts and remains evident over extended electrolysis. This suggests that the catalytic activities arising from the distinct preparations of the oxidation state of Sn in the initial catalyst are separable from evolution of the surface morphology and supports the interpretation that the CO_2-to-formate conversion is strongly influenced by the changes in the initial oxidation state of the SnO_x catalysts.

To better understand how changing the initial oxidation state affects the overall CO_2 reduction activity, additional XPS analysis was performed on the SnO_x catalysts after 1 hr of electrolysis. As shown in the Figure 3A, the O 1s core-level spectra of both samples shows an increase in the higher binding energy peak (~533 eV) with respect to the lower binding energy peak (~531 eV) from pre-electrolysis to post-electrolysis, consistent with some SnO_2 being reduced to SnO during CO_2 electrolysis. Interestingly, despite the reduction in SnO observed after electrolysis in the O 1s spectra on both the catalysts prepared with SnO-rich and SnO_2-rich surfaces, the catalyst prepared with a SnO_2-rich surfaces maintains a distinctive SnO_2 signal even after electrolysis. We hypothesize that lingering presence of strongly-bound O species at the near-surface on the initially SnO-rich surface may have an inductive effect on the Sn site, which facilitates *OCHO binding at the surface rather than *H binding, resulting in enhanced CO_2-to-formate conversion rather than parasitic hydrogen evolution. In addition, the XVBM spectra (shown in Figure 3B) and Sn $3d_{5/2}$ spectra (shown baseline subtracted in Figure S1B and normalized in S2B) suggest some presence of metallic Sn^0 on both SnO_x catalysts after electrolysis which may indicate the existence of Sn/SnO_x interface although the signal at lower binding energy (< ~2.5 eV) in XVBM is possibly from GDL. However, the portion of metallic Sn^0 (Figure S2B) and SnO_2 (Figure S2C) on the surface after electrolysis is remarkably higher for the catalyst prepared with a SnO_2-rich layer. We note that SnO_x layers are known to be robust against full reduction under CO_2 electrolysis conditions.[7,32,33] Thus, the XPS spectra in Figure 3 indicate lasting differences in the characteristic surface chemistry and electronic structure of the catalysts prepared with SnO and SnO_2-rich surfaces. It is worth noting that the correlation between the initial oxidation states of the SnO_x catalysts and the portion of metallic Sn^0 and SnO_x after CO_2 electrolysis is not clear yet, requiring further investigation.

ARTICLE

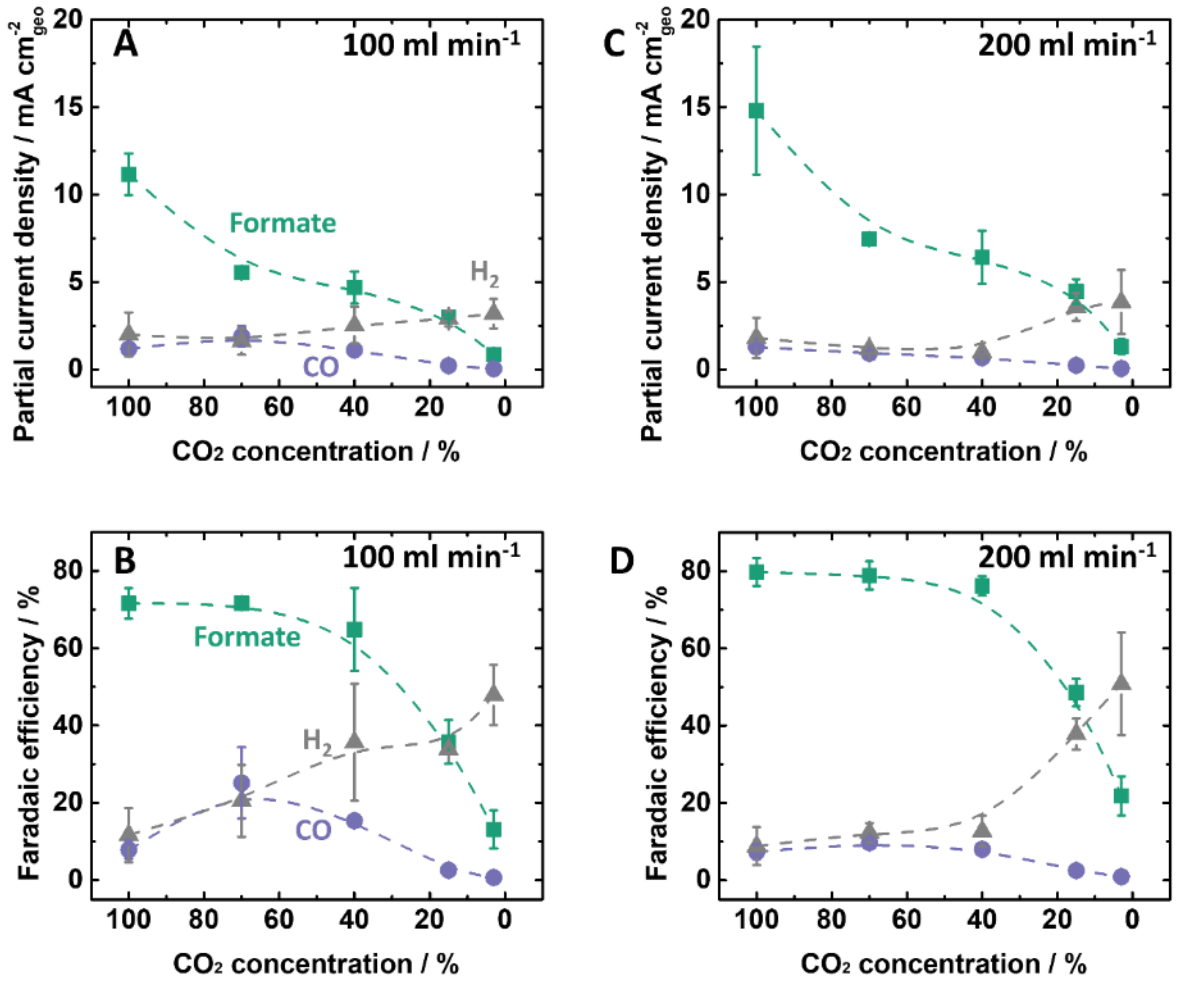

Figure 4. Effect of CO_2 flow rate on the catalytic activity with partially concentrated CO_2 stream. The geometric partial current densities and Faradaic efficiencies of formate (green), CO (purple), and hydrogen (gray) at (A-B) 100 and (C-D) 200 ml min^{-1}, respectively. The CO_2 electrolysis is performed on the SnO-rich catalyst at 3.0 V of cell voltage for 1 hr with a partially concentrated CO_2 stream (3, 15, 40, 70, and 100%).

On the basis of these observations after CO_2 electrolysis, we tentatively speculate that the lower Faradaic efficiency of formate on the catalysts prepared with a SnO_2-rich surface is attributed to the appearance of metallic Sn^0 and remnant SnO_2, consistent with literature.[8,9] The more selective catalyst prepared with a SnO-rich surface exhibits a lower proportion of metallic Sn^0 (Figure S2B) and SnO_2 (Figure S2C) on the surface relative to SnO_2-rich catalysts after electrolysis, suggesting that the presence of metallic Sn^0 coupled with the lack of reduction of SnO_2 is detrimental for CO_2-to-formate reaction. Comparing the core levels (O 1s and Sn $3d_{5/2}$) and XVBM on a Sn metal foil with initial native oxide layer before and after CO_2 electrolysis confirms that 1) the initial native oxide does not fully reduce to Sn^0 during CO_2 electrolysis and 2) the post-electrolysis XPS is sensitive to the changes in the electronic and chemical structure of the SnO_x catalysts rather than re-growth of the oxide layer, as shown in Figure S12. To note, sample transportation between the CO_2 electrolysis and XPS measurement is kept as consistent as possible. The peak appearing at ~537 eV in O 1s spectra in Figure 3A is consistent with bicarbonate salt, confirmed by Raman spectroscopy (Figure S13) and XRD (Figure S6). We note that the unsteady behavior of the current density at the end of

long-term electrolysis in Figure S11 is likely due to unstable clogging of the flow pattern by the bicarbonate salt.

The modest parasitic hydrogen evolution appears to originate from GDL exposure during electrolysis. Increased contact angle of H_2O on the surface of both SnO_x catalysts after CO_2 electrolysis suggests that the agglomerated surface morphology exposes GDL to the surface (Figure S14B-C), which is further confirmed by the energy-dispersive X-ray spectroscopy (SEM-EDS) shown in Figure S15, and XPS results in Figures S1-S3. Furthermore, Figure S16 exhibits that hydrogen is only product on the surface of bare GDL without any formation CO_2 reduction products. We therefore conjecture that the parasitic hydrogen evolution originates from the partial exposure of GDL to the interface between membrane and the surface of gas diffusion electrode (GDE) during electrolysis, slightly reducing the total formate selectivity.

We note that the formate selectivity on the catalysts prepared with a SnO-rich surface in the catholyte-free electrolyzer in this work is comparable to that found in batch-type reactors,[8,10,34] indicating that fundamental insights on the surface chemistry are well applied to the GDE, where an inherently different reaction environment exists.

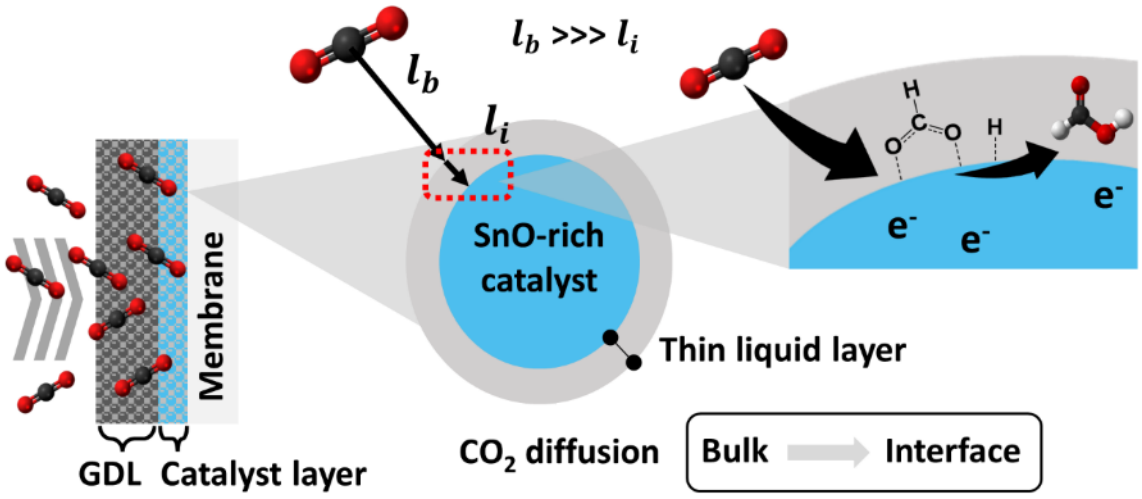

Figure 5. Scheme of the simplified CO_2 mass transportation to the catalyst surface in the catholyte-free electrolyzer. The humidified CO_2 is diffused to the catalyst surface through GDL (bulk) and the thin liquid layer (interface). *OCHO is the reaction intermediate to the formate. l_b and l_i is bulk and internal diffusion path length, respectively.

Effect of CO_2 Concentration and Its Flow Rate on the CO_2 Electrolysis

The CO_2 conversion activity on the catalyst prepared with a SnO-rich surface is curtailed as the concentration of CO_2 stream is reduced from 100% to 3% since the available CO_2 within the vicinity of the catalyst surface is limited, as shown in Figure 4A and C. The geometric partial current density of formate and CO are continuously reduced with decreasing concentration of CO_2 stream while that of hydrogen increases, as shown in Figure 4A. It is known that the electrochemical CO_2 conversion to formate is a first order reaction as the reaction rate is proportional to the CO_2 concentration[35,36] which is consistent with our findings in Figure 4A. The CO generation also appears to be the first order reaction as the geometric partial current density of CO is rather proportional to the CO_2 concentration.

Overall, the partial current density of formate is > 10 times higher than that of CO over the range of CO_2 concentration, which confirms that, regardless of the CO_2 concentration, the CO_2-to-formate reaction is predominant. The CO_2-to-formate reaction is dominantly competing with parasitic hydrogen evolution instead of CO generation. Meanwhile, the hydrogen evolution reaction increases with lower CO_2 concentration, due to the limited mass transport of CO_2.

The Faradaic efficiency of formate is sustained down to 40% CO_2 concentration and substantially suppressed at lower CO_2 concentrations, as shown in Figure 4B. The Faradaic efficiency of formate is sustained with only a marginal decrease at 40% CO_2 concentration (9% and 4% absolute at 100 and 200 ml min^{-1} of flow rate, respectively). In addition, in Figure 4B and D we observe a tradeoff of selectivity between formate and hydrogen, especially below 40% CO_2 concentration, which further emphasizes the importance of facile mass transport of CO_2 in the CO_2-to-formate conversion. We note that the selectivity for CO is suppressed regardless of CO_2 concentration, indicating that the competing reaction on the catalyst prepared with a SnO-rich surface is CO_2-to-formate conversion and parasitic hydrogen evolution rather than CO generation even at the lowest CO_2 concentration (3%).

Increasing flow rate predominantly promotes formate generation and substantially suppresses the CO and hydrogen formation down to 40% CO_2 concentration. Increasing flow rate of the pure and partially concentrated CO_2 stream from 100 to 200 ml min^{-1} results in ~1.4x higher partial current density of formate and ~10% reduction in the partial current densities of

CO and hydrogen, down to 40% CO_2 concentration as shown in Figure 4C. Similarly, with an increase in flow rate of CO_2, we observe ~1.3x increase in formate Faradaic efficiency and a 20% decrease in Faradaic efficiency for CO and hydrogen, as shown in Figure 4D. We note that the Faradaic efficiencies of CO and hydrogen at 200 ml min^{-1} of CO_2 flow rate in Figure 4D are below about 10% when CO_2 concentration is 40% or above, with substantial suppression of these alternative products relative to the electrolysis 100 ml min^{-1} (Figure 4B). To exclude the effect of the overpotential on the overall activity, the cell voltage was maintained at 3.0 V for these flow studies. Although a tradeoff in selectivity remains between formate and hydrogen below 40% CO_2 concentrations regardless of the CO_2 flow rate, we speculate that the improved formate activity at the higher flow rate can be largely attributed to the mass transport of CO_2 to the catalytic sites. Possibly, the increased flow rate of CO_2 helps the diffusion of the generated formate away from the catalyst surface to the flow field, which simultaneously facilitates CO_2 transport to the catalytic sites.[18]

It is important to determine the rate limiting step that governs overall CO_2 reduction activity to understand the effect of increasing the CO_2 flow rate. Adopting a three-phase interface model of CO_2(g)-aqueous medium(l)-catalyst(s) in our CO_2 conversion system, the CO_2 must diffuse through both the GDL and a very thin liquid layer to reach to the catalyst surface as shown in Figure 5. In general, a thin layer of water is suggested to be present on the surface of catalyst in the catholyte-free electrolzyer due to osmotic drag through membrane.[18,20] That water crosses over from the anode to the cathode side especially in the catholyte-free electrolyzer is well established.[18,20,37] At the three-phase interface of CO_2 reduction, the current density is approximately proportional to the CO_2 mass transfer flux, which is a function of mass transfer coefficient and the CO_2 concentration gradient from bulk to the surface.[38,39] Considering the negligibly short internal diffusion length (l_i) relative to bulk diffusion length (l_b), as shown in Figure 5, and the high diffusion coefficient of humidified CO_2 in the three-phase interface system as compared to the two-phase interface system (electrolyte(l)-catalyst(s), typically in the batch-type reactor),[40] it is assumed that the CO_2 mass transfer flux in the gas phase is identical to that in the liquid. This means that the internal CO_2 mass transport through the thin liquid layer may not particularly be the reaction limiting step. Instead, we suggest that the entire CO_2 mass transport from bulk to the catalytic sites (l_b+l_i) is to be rate limiting. This is consistent with the works of Shi et al., who compared the local CO_2 concentration at the biased catalyst surface between the three-phase (gas-phase CO_2 feed) and the double-phase (solubilized CO_2 feed) interface systems. They emphasize that the CO_2 transportation from the bulk gas phase results in a fast recovery of CO_2 deficiency on the catalytic sites even at high current density (> 50 mA cm^{-2}). This transport is a key factor of the overall CO_2 reduction activity, suggesting that the entire CO_2 mass transport from bulk to the catalytic sites is the reaction limiting step.[38] In addition, we note that it is theoretically expected that increasing CO_2 flow rate results in increasing mass transfer coefficient and consequently enhanced overall CO_2 reduction activity.[39] This further supports that reaction kinetics of formate generation can be improved with facile CO_2 mass transport. Overall, we conclude that the rapid mass transport of CO_2 remains a critical factor of designing CO_2 electrolysis system to enhance CO_2 conversion activity.

Conclusions

In summary, the selectivity and energy efficiency of the electrochemical CO_2 conversion to formate in catholyte-free electrolyzers can be enhanced via controlling the initial chemical state of Sn species on SnO_x catalysts. An improved formate selectivity (83% FE) is observed on the catalyst containing a mixture of SnO and SnO_2, which leads to 36% of energy efficiency for formate generation at 3.0 V of cell voltage, offering the potential for net negative CO_2 conversion using existing grids with large penetration of renewables (e.g. California). Also, we find that increasing CO_2 flow rate enhances reaction kinetics toward formate generation, even at partial concentration CO_2 stream in the catholyte-free electrolyzer, which confirms that sufficient CO_2 mass transport to the catalytic site is a critical design parameter for CO_2 electrolysis reactor. These findings showcase the importance of controlling chemical state of the catalyst and facile mass transport of CO_2 to achieve carbon negative electrochemical CO_2 conversion system.

Experimental

Electrode preparation

To prepare SnO_x electrodes, SnO_2 nanoparticles (99.7% purity, 35-55 nm, US Research Nanomaterials) are placed in an alumina-coated tungsten boat in a high vacuum (< $7x10^{-7}$ mbar) chamber for thermal evaporation at a rate of 0.14-0.2 $\dot{A}$ s^{-1} onto GDLs. GDLs are purchased from Fuelcellstore (AvCarb GDS2230) and cut into 1 cm^2 sized pieces. The cut GDLs are used with no further pre-treatment. To note, the film thickness is selected based on an initial assessment to optimize the CO_2 electrolysis performance (i.e., geometric current density and selectivity). Furthermore, in order to achieve the accuracy and reproducibility of the film thickness, the thickness of the SnO_x layers is strictly monitored via quartz crystal microbalance (QCM) and a J.A. Woollam M-2000D spectroscopic ellipsometer, giving sub-nanometer standard deviation and thus a highly reproducible sample preparation. For the post-heat treatment, the as-prepared electrodes are annealed at 300 ^oC for 5 hrs in a muffle furnace, which eventually transforms the initially SnO-rich surface due to oxygen deficiency to SnO_2-rich surface. Further details can be found in our previous work.[25] The surface morphologies of the as-prepared electrodes are characterized by scanning electron microscopy (SEM, Zeiss, Sigma 500). Surface valence band and core-level electronic structure of the as-prepared electrode are characterized by X-ray photoelectron spectroscopy (XPS) with a 90° emission angle with respect to electrode surface (Kratos, AXIS Supra) using monochromatic Al Kα radiations at vacuum levels below $5x10^{-8}$

Torr. The XPS spectra are recorded using pass energies of 160 eV for the XPS survey and 20 eV for the core-level scans. The valence band spectra are recorded using pass energy of 40 eV. The binding energies are calibrated using both Fermi edge (−0.06 eV) and the Au 4 $f_{7/2}$ second-order peak (84 eV). The IrO_x anode is prepared via modified thermal pyrolysis.[41,42] Surface-etched Ti meshes (Fuelcellstore) are used as substrates. The meshes are cut into 1 cm^2 sized pieces that are sonicated in a mixture of acetone/IPA/DI water (6:3:1 v/v), followed by DI water for 10 min each. The cleaned substrates are etched in 20 vol.% of HCl solution for 5 min and then transferred to 10 wt.% boiling oxalic acid solution for 10 min prior to final cleaning with DI water in a bath sonication. A precursor solution is prepared by dissolving 26 mg of Iridium (III) chloride hydrate (99.9% purity, Sigma Aldrich) in a mixture of 6.71 ml IPA and 2 ml of concentrated HCl solution. The precursor solution is subsequently dropped onto surface-etched Ti meshes that are pre-heated to 125 ^oC until the total loading of 1.0 mg cm^{-2} is achieved. The electrodes are finally annealed at 500 ^oC for 3 hrs in a muffle furnace. The contact angles of H_2O are measured using a Goniometer (rame-hartTM Model 200). The structure of the SnO_x catalysts layers is characterized by X-ray diffractometry (XRD, Anton Paar, XRDynamic 500) in a parallel beam configuration with an incident beam fixed at 5 degrees on glass, and before and after electrolysis on the GDL.

Electrolyzer configuration

A customized catholyte-free electrolyzer (Fuel Cell Technologies, Inc) with an active area of 1 cm^2 is used for all CO_2 electrolysis. In contrast to the MEA commonly found in fuel cells with no anolyte nor catholyte, here we adopt a catholyte-free electrolyzer[18,37,43] such that the CO_2 remains undiluted at the cathode but oxygen is evolved from an acidic anolyte. The interdigitated flow channels are applied to both graphite and Ti current collectors (for cathode and anode, respectively). A Nafion 117 is used as a proton exchange membrane. IrO_x on Ti mesh electrodes are used as anode. To estimate overpotential on the anode, Ag/AgCl (KCl gel) reference electrode is incorporated using a customized acrylic spacer between the membrane and the anode. The calculated overpotential of the anode is approximately 550 mV at 50 mA/cm_{geo}^2 (Figure S17). Prior to CO_2 electrolysis, the membrane is rinsed and sonicated with DI water, and then immersed in the anolyte solution at least overnight. PTFE sheets (0.01 inch) were used as gaskets. The electrolzyer is compressed with 8 hex screws sequentially torqued (8-10-12 N m) with an electronic torque wrench.

Carbon Dioxide electrolysis

The electrochemical analysis is performed in the two-electrode system using a potentiostat (VSP-300, biologic). Prepared cathodes, the Nafion membrane, and IrO_x anode are positioned and sandwiched together via current collectors with PTFE gaskets. 40 ml of 0.5 M sodium phosphate buffer (98% purity, Fisher scientific) solution (pH 3) is circulated using a peristaltic pump through the backside of the Ti flow channels on the anode side. Research-grade CO_2 gas is supplied to the backside of the graphite flow channels on the cathode side through a home-made bubbler setup at the rate of 200 ml min^{-1} unless otherwise mentioned. The flow rate is controlled by a mass flow controller (Smart Track 100, Sierra). The partially concentrated CO_2 stream (from 3 to 70% of CO_2) is formulated by mixing using mass flow controllers with research-grade N_2 gas. At least three electrolyses are carried out at each experimental condition for repeatability. CO_2 electrolysis on the untreated Sn metal foil (99.998% purity, Alfa Aesar) is also performed in 3 electrode system in a batch reactor, which consists of untreated Sn foil, graphite rod, and Ag/AgCl/KCl(gel) as a working, counter, and reference electrode, respectively. CO_2-saturated 0.1 M $KHCO_3$ at 5 sccm of CO_2 flow rate is used as electrolyte. Online quantification for gas products is started after 20 min of initial electrolysis to account for any stabilization of the cathode. All gas products produced from the cathode are collected directly into a gas-sampling loop and quantified by gas chromatography (GC, SRI 8610C, SRI) with a molecular sieve of 5A and a Haysep D column, a TCD/FID detector equipped with a methanizer, and using Ar as a carrier gas. The partial current density of each gas product is averaged over 4 GC injections during 1 hr electrolysis with chronoamperometry. The liquid product is quantified at the end of each electrolysis using ^1H nuclear magnetic resonance (NMR) spectroscopy with a 500 MHz spectrometer (ECA500, JEOL). The water peak is suppressed via a presaturation sequence. Additional details on quantification can be found in our previous work.[44] Raman analysis is applied to identify salt after 1 hr of CO_2 electrolysis. Raman spectra are taken on an inVia confocal Raman microscope (Renishaw) using a 633 nm excitation laser and 600 l/mm. Each spectrum is summed from 25 scans across a 2x2 mm^2 area with 2 seconds of exposure per scan.

Author Contributions

T.K conceived the idea, performed experiments, analyzed data, and wrote the manuscript. V.S.D. and S.D. contributed to experiments. A.G. contributed to sample preparation. S.P.D., M.K., and J.R.P contributed to characterization. D.P.F. helped T.K. formulate the idea, supervised the research, data analysis, and writing. All authors have given approval to the final version of the manuscript.

Conflicts of interest

There are no conflicts to declare.

Acknowledgements

This work was supported by the UC Office of the President's Carbon Neutrality Initiative Applied Research Pillar. This work was performed in part at the San Diego Nanotechnology Infrastructure (SDNI) of UCSD, a member of the National Nanotechnology Coordinated Infrastructure, which is

supported by the National Science Foundation (Grant ECCS-1542148). The authors acknowledge the use of facilities and instrumentation at the UC Irvine Materials Research Institute (IMRI), which is supported in part by the National Science Foundation through the UC Irvine Materials Research Science and Engineering Center (DMR-2011967). The authors thank Dr. Ich C. Tran for XPS measurement and Louis Ah for thickness measurement.

References

1 M. B. Ross, P. De Luna, Y. Li, C. T. Dinh, D. Kim, P. Yang and E. H. Sargent, *Nat. Catal.*, 2019, **2**, 648–658.

2 G. Li, T. Yan, X. Chen, H. Liu, S. Zhang and X. Ma, *Energy & Fuels*, 2022, **36**, 4234–4249.

3 P. De Luna, C. Hahn, D. Higgins, S. A. Jaffer, T. F. Jaramillo and E. H. Sargent, *Science (80-.).*, , DOI:10.1126/science.aav3506.

4 Z. Ma, U. Legrand, E. Pahija, J. R. Tavares and D. C. Boffito, *Ind. Eng. Chem. Res.*, 2021, **60**, 803–815.

5 J. T. Feaster, C. Shi, E. R. Cave, T. Hatsukade, D. N. Abram, K. P. Kuhl, C. Hahn, J. K. Nørskov and T. F. Jaramillo, *ACS Catal.*, 2017, **7**, 4822–4827.

6 C. Oloman and H. Li, *ChemSusChem*, 2008, **1**, 385–391.

7 Y. Chen and M. W. Kanan, *J. Am. Chem. Soc.*, 2012, **134**, 1986–1989.

8 A. Dutta, A. Kuzume, M. Rahaman, S. Vesztergom and P. Broekmann, *ACS Catal.*, 2015, **5**, 7498–7502.

9 J. E. Pander, M. F. Baruch and A. B. Bocarsly, *ACS Catal.*, 2016, **6**, 7824–7833.

10 X. An, S. Li, A. Yoshida, Z. Wang, X. Hao, A. Abudula and G. Guan, *ACS Sustain. Chem. Eng.*, 2019, **7**, 9360–9368.

11 S. Nitopi, E. Bertheussen, S. B. Scott, X. Liu, A. K. Engstfeld, S. Horch, B. Seger, I. E. L. Stephens, K. Chan, C. Hahn, J. K. Nørskov, T. F. Jaramillo and I. Chorkendorff, *Chem. Rev.*, 2019, **119**, 7610–7672.

12 J. T. Billy and A. C. Co, *ACS Catal.*, 2017, **7**, 8467–8479.

13 R. F. Weiss, *Mar. Chem.*, 1974, **2**, 203–215.

14 D. Higgins, C. Hahn, C. Xiang, T. F. Jaramillo and A. Z. Weber, *ACS Energy Lett.*, 2019, **4**, 317–324.

15 K. Liu, W. A. Smith and T. Burdyny, *ACS Energy Lett.*, 2019, **4**, 639–643.

16 Z. Z. Niu, F. Y. Gao, X. L. Zhang, P. P. Yang, R. Liu, L. P. Chi, Z. Z. Wu, S. Qin, X. Yu and M. R. Gao, *J. Am. Chem. Soc.*, 2021, **143**, 8011–8021.

17 Z. Z. Niu, L. P. Chi, R. Liu, Z. Chen and M. R. Gao, *Energy Environ. Sci.*, 2021, **14**, 4169–4176.

18 W. Lee, Y. E. Kim, M. H. Youn, S. K. Jeong and K. T. Park, *Angew. Chemie*, 2018, **130**, 6999–7003.

19 D. Kim, W. Choi, H. W. Lee, S. Y. Lee, Y. Choi, D. K. Lee, W. Kim, J. Na, U. Lee, Y. J. Hwang and D. H. Won, *ACS Energy Lett.*, 2021, **6**, 3488–3495.

20 D. S. Ripatti, T. R. Veltman and M. W. Kanan, *Joule*, 2019, **3**, 240–256.

21 C. Xia, P. Zhu, Q. Jiang, Y. Pan, W. Liang, E. Stavitski, H. N. Alshareef and H. Wang, *Nat. Energy*, 2019, **4**, 776–785.

22 U. Legrand, U.-P. Apfel, D. C. Boffito and J. R. Tavares, *J. CO2 Util.*, 2020, **42**, 101315.

23 F. A. Akgul, C. Gumus, A. O. Er, A. H. Farha, G. Akgul, Y. Ufuktepe and Z. Liu, *J. Alloys Compd.*, 2013, **579**, 50–56.

24 J. Haeberle, S. Machulik, C. Janowitz, R. Manzke, D. Gaspar, P. Barquinha and D. Schmeißer, *J. Appl. Phys.*, 2016, **120**, 105101.

25 M. Kodur, Z. Dorfman, R. A. Kerner, J. H. Skaggs, T. Kim, S. P. Dunfield, A. Palmstrom, J. J. Berry and D. P. Fenning, *ACS Energy Lett.*, 2022, **7**, 683–689.

26 X. S. Peng, G. W. Meng, X. F. Wang, Y. W. Wang, J. Zhang, X. Liu and L. D. Zhang, *Chem. Mater.*, 2002, **14**, 4490–4493.

27 J. G. Partridge, M. R. Field, J. L. Peng, A. Z. Sadek, K. Kalantar-zadeh, J. Du Plessis and D. G. McCulloch, *Nanotechnology*, 2008, **19**, 125504.

28 B. Zhang, Y. Yu, Z. Huang, Y. B. He, D. Jang, W. S. Yoon, Y. W. Mai, F. Kang and J. K. Kim, *Energy Environ. Sci.*, 2012, **5**, 9895–9902.

29 Q. Yin, F. Gao, J. Wang, Z. Gu, E. A. Stach and G. Zhou, *J. Mater. Res.*, 2017, **32**, 1194–1202.

30 Z. Wang, Y. Zhou, C. Xia, W. Guo, B. You and B. Y. Xia, *Angew. Chemie Int. Ed.*, 2021, **60**, 19107–19112.

31 California Independent System Operator, California ISO - Emissions, https://www.caiso.com/TodaysOutlook/Pages/emissions.aspx, (accessed 15 June 2022).

32 C. Huo, X. Cao, Z. Ye, Y. Li and T. Lu, *ChemCatChem*, 2021, **13**, 4931–4936.

33 T. Yuan, Z. Hu, Y. Zhao, J. Fang, J. Lv, Q. Zhang, Z. Zhuang, L. Gu and S. Hu, *Nano Lett.*, 2020, **20**, 2916–2922.

34 Q. Zhang, Y. Zhang, J. Mao, J. Liu, Y. Zhou, D. Guay and J. Qiao, *ChemSusChem*, 2019, **12**, 1443–1450.

35 S. Zhang, P. Kang and T. J. Meyer, *J. Am. Chem. Soc.*, 2014, **136**, 1734–1737.

36 X. Min and M. W. Kanan, *J. Am. Chem. Soc.*, 2015, **137**, 4701–4708.

37 W. Choi, S. Park, W. Jung, D. H. Won, J. Na and Y. J. Hwang, *ACS Energy Lett.*, 2022, **7**, 939–945.

38 R. Shi, J. Guo, X. Zhang, G. I. N. Waterhouse, Z. Han, Y. Zhao, L. Shang, C. Zhou, L. Jiang and T. Zhang, *Nat. Commun.*, 2020, **11**, 1–10.

39 H. Scott Fogler, *Elements of Chemical Reaction Engineering*, Pearson, 4th edn., 2006.

40 L.-C. Weng, A. T. Bell and A. Z. Weber, *Phys. Chem. Chem. Phys.*, 2018, **20**, 16973–16984.

41 J. Li, A. Ozden, M. Wan, Y. Hu, F. Li, Y. Wang, R. R. Zamani, D. Ren, Z. Wang, Y. Xu, D.-H. Nam, J. Wicks, B. Chen, X. Wang, M. Luo, M. Graetzel, F. Che, E. H. Sargent and D. Sinton, *Nat. Commun.*, 2021, **12**, 2808.

42 T. Kim, G.-P. Kim, D. Lee, Y. Kim, S. E. Shim and S. Baeck, *J. Nanosci. Nanotechnol.*, 2016, **16**, 10892–10897.

43 B. De Mot, M. Ramdin, J. Hereijgers, T. J. H. Vlugt and T. Breugelmans, *ChemElectroChem*, 2020, **7**, 3839–3843.

44 T. Kim, R. E. Kumar, J. A. Brock, E. E. Fullerton and D. P. Fenning, *ACS Catal.*, 2021, **11**, 6662–6671.